A THREE-DIMENSIONAL SIMULATION OF SEISMIC WAVES IN THE SANTA CLARA VALLEY, CALIFORNIA, FROM A LOMA PRIETA AFTERSHOCK

By Arthur Frankel and John Vidale

Abstract

The finite-difference method is used to propagate elastic waves through a 3-D model of the Santa Clara Valley, an alluvium-filled basin that underlies the city of San Jose, California. The model was based on depth to bedrock information from water wells in the area. The simulation corresponded to a region 30 (east–west) by 22 (north–south) by 6 (depth) km and contained about 4 million grid points. Synthetic seismograms from the simulation are accurate at frequencies up to 1 Hz. Motions from a magnitude 4.4 aftershock of the Loma Prieta earthquake were modeled. Snapshots of ground motion and synthetic seismograms from the simulation are presented. The simulation illustrates S-to-surface-wave conversion at the edges of the basin and the large amplitude and long duration of ground motion in the basin compared to the surrounding rock. Love waves produced at the edge of the basin are the largest arrivals in the transverse synthetics. Because of the slow group velocity of the Love waves, sites near the center of the basin have longer durations of significant motions than basin sites near the valley edges. Sites near the center of the basin also show larger peak amplitudes on the transverse component. Array analysis of the synthetic seismograms indicates that Love waves tend to propagate parallel to the eastern and western edges of the valley. Rayleigh waves are produced along the southern margin of the basin from incident S waves. Large radial motions occur where a Rayleigh wave impinges on the northeast margin of the valley. Some Rayleigh waves travel westward across the basin, after being scattered from the eastern edge of the valley. Synthetic seismograms from the simulation have similar peak amplitudes as seismograms recorded by the Sunnyvale dense array for this aftershock, although the duration of the transverse component is not matched by the synthetic seismogram, using this basin model. The simulation indicates that the Love waves observed on the actual seismograms were produced by conversion of incident S waves at the southern margin of the Santa Clara Valley. 2-D simulations show how the S-to-Love-wave conversion is affected by the angle of incidence of the S wave and the sharpness of the velocity transition between the alluvium and bedrock. As more accurate basin models are developed, 3-D simulations should become valuable for predicting ground motions in sedimentary basins for future large earthquakes.

Introduction

With the increased speed and memory of computers, large-scale numerical simulations involving 3-D variations in crustal structure are now feasible. There are a myriad of seismological applications for such 3-D simulations. In this paper, we consider one of them: the propagation of seismic waves in sedimentary basins. Many population centers are situated in sedimentary basins near the rupture zones of expected large earthquakes. It is well known that sites in sedimentary basins experience larger ground motions with longer durations than do sites on rock (e.g., Borcherdt and Gibbs, 1976). However, modeling of shaking in basins has been largely limited to crustal models that

vary in one or two dimensions. 1-D crustal models (horizontal plane layers) show the effects of multiple reverberations of body waves in the sedimentary layers (Kanai, 1952; Haskell, 1960). Numerical simulations for media with velocity variations in two dimensions have demonstrated the importance of S wave to surface-wave conversion at the edges of basins (Aki and Larner, 1970; Bard and Bouchon, 1980a, b, 1985; Harmsen and Harding, 1981; Ohtsuki and Harumi, 1983; Bard et al., 1988; Vidale and Helmberger, 1988; Kawase and Aki, 1989). These surface waves can substantially increase the duration and amplitude of shaking for sites in the basin, relative to that expected from a horizontal plane layer over a half-space. It has been suggested that such surface waves were responsible for much of the damage to Mexico City in the 1985 earthquake (Kawase and Aki, 1989). There has been some work on 3-D wave propagation for simple symmetric basin models (e.g., Sánchez-Sesma, 1983; Rial, 1989; Sánchez-Sesma et al., 1989).

Ultimately, 3-D simulations will be used to predict seismic shaking in sedimentary basins for future large earthquakes. Accurate prediction of ground motions in basins requires 3-D simulations for several reasons. Lateral variations in sediment thickness and velocity could cause site response to be dependent on the azimuth to the earthquake. In closed basins, resonant modes can be set up by waves multiply reflected by the edges of the basin (Rial, 1989). In addition, the 3-D curvature of the alluvium-basement interface could cause focusing of body waves for certain locations in the basin. For irregularly shaped basins, S-to-surface-wave conversion could occur along several portions of the border of the basin, producing surface waves travelling in different directions across the basin. 3-D simulations would also be useful for studying shaking from extended ruptures, where the azimith and angle of incidence of S waves impinging on a basin varies for waves from different parts of the rupture zone.

This paper applies a 3-D finite-difference computer program to propagate seismic waves in the Santa Clara Valley, California (Fig. 1), an alluvium-filled basin south of San Francisco. This area was chosen partly because recordings of aftershocks of the 1989 Loma Prieta earthquake were available from a small-aperture array located in this valley. Analysis of seismograms from the Sunnyvale dense array revealed that large motions after the S wave were produced by surface waves travelling in the basin (Frankel et al., 1991). Much of the surface-wave energy was propagating from directions substantially different from the direction to the source, indicating that it had been scattered from the edges of the basin. The presence of off-azimuth arrivals emphasizes the need to use a 3-D model of the basin to model the observed waveforms. This portion of the Santa Clara Valley contains the city of San Jose and is a major population center. This area is also important because of its substantial computer-related industry and is often referred to as "Silicon Valley." Obviously, understanding and predicting earthquake ground motions in this valley are important to society.

We simulated the seismic wave field produced by the Loma Prieta aftershock designated as event 1 by Frankel et al. (1991) that was recorded on the Sunnyvale dense array. This M_L 4.4 aftershock occurred on 25 October 1989 at 1:27 UT (see Fig. 1) and had a source depth of 10.2 km. This event exhibited a large Love wave at the dense array that could not be explained by a plane-layered velocity model. Many of the arrivals following the S wave for this event had backazimuths substantially more to the east than the epicenter.
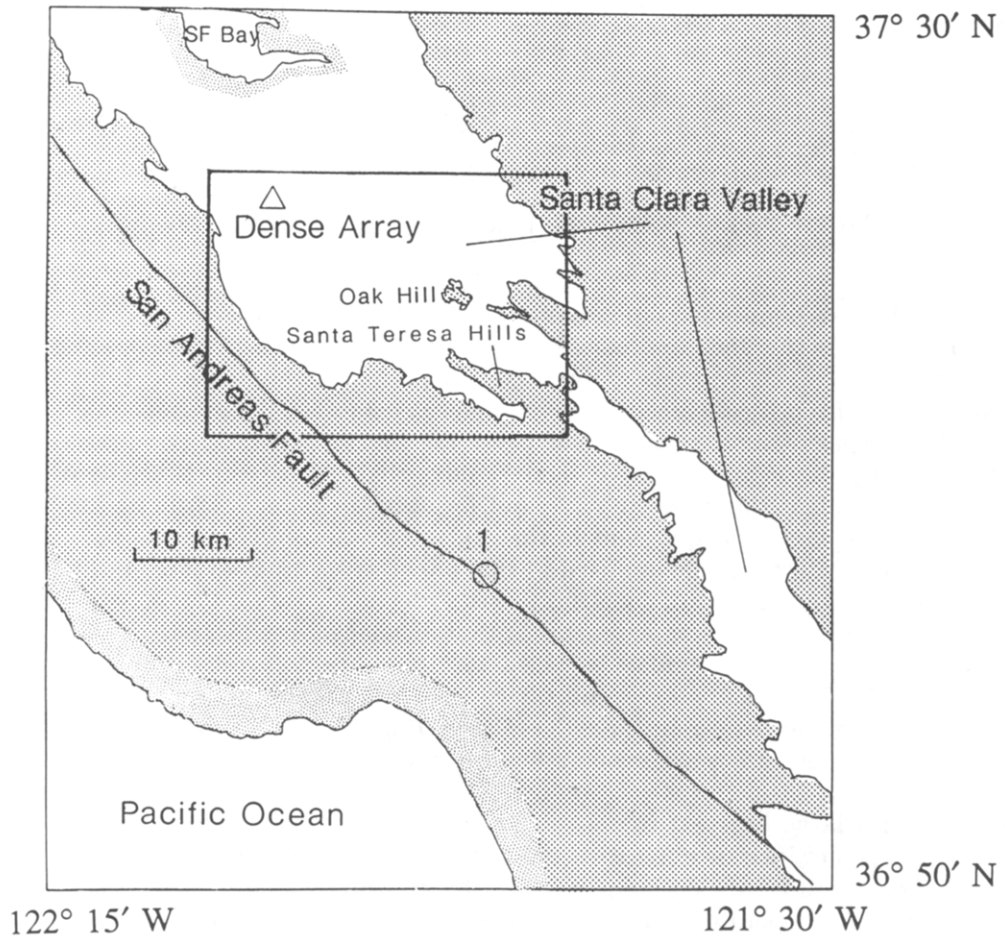
FIG. 1. Map showing location of the Santa Clara valley, position of Sunnyvale dense array (triangle), and epicenter (circle) of aftershock modeled by the 3-D simulation. The boundary of the Santa Clara valley is the contact between alluvium and consolidated rock (from California Division of Mines and Geology, 1969). Shading indicates bedrock at the surface (except for stippling around San Francisco Bay). Box shows area used in the 3-D simulation.

We use the 3-D Santa Clara valley simulation to illustrate the types of effects that occur in irregularly shaped sedimentary basins. Specifically, we seek to explain observations from the Sunnyvale dense array, such as the large surface waves and the presence of off-azimuth arrivals.

METHOD

The 3-D finite-difference method propagates the complete elastic wave field in a medium with arbitrarily complicated velocity structure. This wave field includes P-to-S, S-to-P, body-to-surface, and surface-to-body-wave conversions, as well as head waves, diffractions, and multiple scattering. A general discussion of the finite difference method for 2-D media is provided in Kelly et $al.$ (1976). For the 3-D case, let u, v, w be the displacements in the x, y, z directions, respectively. ρ denotes density and λ and μ are the Lamé constants. These medium properties vary with position. The three coupled wave equations

are:

$$\rho u_{tt} = \left[(\lambda + 2\mu)u_x + \lambda w_z + \lambda v_y \right]_x + \left[\mu u_y + \mu v_x \right]_y + \left[\mu u_z + \mu w_x \right]_z,$$

$$\rho v_{tt} = \left[(\lambda + 2\mu)v_y + \lambda w_z + \lambda u_x \right]_y + \left[\mu v_x + \mu u_y \right]_x + \left[\mu v_z + \mu w_y \right]_z,$$

$$\rho w_{tt} = \left[(\lambda + 2\mu)w_z + \lambda u_x + \lambda v_y \right]_z + \left[\mu w_x + \mu u_z \right]_x + \left[\mu w_y + \mu v_z \right]_y.$$

Here subscripts denote partial derivatives. The partial derivatives are replaced by their finite-difference approximations for a 3-D grid with equal spacing in x, y, and z. At each grid point, the vector displacement for the next time step can be found from the displacements at adjacent points for the present time step and the displacements at that grid point for the present and previous time steps. Thus, the complete wave field is advanced in discrete time steps by applying the algorithm at each grid point for each time step. Synthetic seismograms can be saved for any point in the grid.

The finite-difference scheme used in this paper is accurate to fourth-order in space and second-order in time. The fourth-order algorithm that approximates the spatial derivatives is an extension of that developed by Vidale (1990) for the 2-D case. Absorbing boundaries based on those described by Clayton and Engquist (1977) were applied on all sides of the grid except the top. A one-sided difference scheme (Alterman and Rotenberg, 1969) was used for the free surface. A two-sided difference scheme for the free surface (Alterman and Karal, 1968) was found to be unstable for the case of a layer over a half-space when there was a large contrast in seismic velocity across the interface. The above equations do not include anelastic attentuation. Later in this paper, we approximate the effects of anelastic attenuation by convolving the synthetic seismograms with a Q operator that varies with time (Vidale and Helmberger, 1988).

The grid size for the Santa Clara Valley simulation was 300 points in the east–west direction, 220 points in the north–south direction, and 60 points in the vertical direction. The grid spacing used was 100 m, so that the simulation corresponded to 30 by 22 by 6 km in depth. There are 3.96 million grid points. The displacements (three components) at two time steps are continually saved, requiring 23.76 million words of memory. Additional CPU memory is required for the medium parameters. The code was vectorized for use on the Cray. We achieved a speed of about 6 sec per time step. Each time step represented 0.015 sec. The simulation was for 3000 time steps, corresponding to 45 sec. This run required about 5 hours of CPU time on the Cray YMP at the University of California, San Diego.

We were particularly concerned with the accuracy of the 3-D code for the case of a basin with a relatively thin sedimentary fill. The Santa Clara Valley has a large horizontal extent compared to its thickness. Although it is not known precisely, the maximum thickness of the sediments is thought to be about 500 m (E. Helley, personal comm., 1990). With a grid spacing of 100 m, the maximum thickness of the sediments is only five grid points. To evaluate the accuracy of the 3-D code for such thin layers, we considered the case of a thin horizontal layer over a half-space. Synthetic seismograms from the 3-D finite-difference method were compared to those generated by the reflectivity method of Saikia and Sen (1989), which does not have the numerical inaccuracies of the

finite-difference method. Both methods include near-field terms in the synthetics.

We calculated synthetic seismograms for a model with a low-velocity surface layer ($V_P = 1.1$ km/sec, $V_S = 0.6$ km/sec, $\rho = 2.0$ gm/cc) over a half-space ($V_P = 3.5$ km/sec, $V_S = 2.0$ km/sec, $\rho = 2.6$ gm/cc). These are the same velocities used later in the Santa Clara Valley simulation. The low velocity was assigned to the top four grid levels in the model, starting at the free surface. The grid spacing was 100 m, the same as used in the Santa Clara simulation. Since interfaces in the finite-difference scheme are located halfway between grid points, we would expect the finite-difference model to correspond to a 400-m-thick surface layer. The reflectivity synthetics were computed for a layer thickness of 400 m. The source was at a depth of 1 km, and the receiver was at an epicentral distance of 3 km. Two cases were considered: an explosion and a strike-slip earthquake with vertical dip and strike perpendicular to the azimuth to the receiver. The source was inserted in the grid by specifying displacements at the grid points adjacent to the source location. These displacements correspond to the equivalent force system appropriate to that type of source. For the explosion these are outward-directed displacements specified at the six points surrounding the source location. Two force couples are required for the strike-slip earthquake. For each method, the source time function was an isosceles triangle with a base of 1.0 sec. The synthetics for each method were low-pass filtered with a corner at 1.0 Hz. We used a high Q of 2500 for the reflectivity run, since the 3-D simulation does not include anelasticity.

Figure 2 shows the synthetic velocity seismograms derived from the 3-D finite-difference code and the reflectivity method, for the explosion (radial and vertical synthetics) and strike-slip earthquake (transverse synthetic). For the explosion, the radial synthetics are very similar in both shape and amplitude for the two methods (Fig. 2, *left*). The vertical synthetics for the explosion start off very similar in amplitude and waveform, for the S wave (Fig. 2, *center*). On this component, there is a progressive delay of the peaks in the Rayleigh wave in the finite-difference synthetic compared to the reflectivity synthetic, with increasing time in the records. By the end of the seismogram, a peak of the Rayleigh wave is arriving about 1.5 sec later on the finite-difference synthetic than on the reflectivity synthetic. This is probably caused by grid dispersion in the finite-difference method, which tends to reduce the propagation speed of waves in the grid (see Alford *et al.*, 1974).

There is generally good agreement between the two methods for the transverse velocity waveforms for a strike-slip earthquake (Fig. 2, *right*). The peak
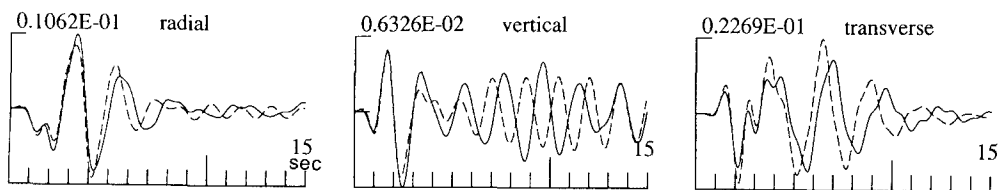

FIG. 2. Comparison of radial (*left*) and vertical (*center*) synthetic seismograms between the 3-D finite-difference code and the reflectivity method, for an explosion source. Reflectivity synthetics are dashed lines, finite-difference synthetics are solid lines. (*Right*) Comparison of transverse (*SH*) synthetics from both methods for a strike-slip earthquake. Model is a 400-m-thick horizontal layer over a half-space, with the source at 1 km depth. Epicentral distance is 3 km.

amplitude of the finite-difference synthetic is about 80% that of the reflectivity synthetic. The long-period Love waves are delayed somewhat in the finite-difference synthetic compared to the reflectivity waveform. Again this delay increases with increasing time in the record and reaches about 1 sec by about 10 sec into the record (Fig. 2, *right*). This delay is likely due to grid dispersion from the finite-difference method. From these synthetics, we estimate that grid dispersion produces an error of about 10% in the velocity of the slow Rayleigh waves and Love waves in the finite-difference simulations. Thus, the synthetic seismograms shown in this paper probably overestimate the total duration of motion by about 10%.

Despite having a surface layer only four grid points thick, the finite-difference method produces synthetics comparable to the reflectivity method. These comparisons indicate that the synthetics for the finite-difference code are sufficiently accurate up to frequencies of about 1 Hz, for the purposes of this paper. One Hz corresponds to a wavelength of six grid points for shear waves in the alluvium. A wavelength to grid spacing ratio of six is near the minimum needed to achieve adequate accuracy for a 2-D fourth-order finite-difference code, according to Alford *et al.* (1974). Of course, the "accuracy" of the finite difference synthetics to actual data is also determined by the accuracy of the velocity model to the true velocities.

3-D MODEL OF THE SANTA CLARA VALLEY

A major obstacle to applying the 3-D code to actual basins is the lack of detailed velocity models for most basins. In areas without extensive oil exploration, the thickness of the alluvium in deep basins is often unknown. To produce a 3-D model of the Santa Clara Valley we used depth to bedrock data from water wells. Figure 3 shows the locations of the water wells used and the depth to bedrock for each well (California Department of Water Resources, 1967). The depth to bedrock is largely unknown in the central portion of the valley, since water wells do not reach bedrock there. We assigned an alluvium thickness of 1500 feet (457 m) for points near the center of the valley, consistent with the conjectured contour for this thickness from California Department of Water Resources (1967). A depth of 400 m was specified under the Sunnyvale dense array location, based on the depth of nearby wells. The location of the dense array is labeled as SUN in Figure 3. In a few cases, the depth to bedrock was approximated as the depth of the well, even if it did not reach bedrock. A minimum-tension surface was fit to the basement depths from the well data and the assigned depth points. This surface was used to interpolate the alluvium thickness to the grid of points used in the simulation. Figure 3 also depicts the resulting depth contours of the alluvium-rock interface used in the 3-D simulation.

We used a simple two-component velocity model consisting of one set of velocities for rock and one set for alluvium. Given the absence of detailed velocity information in the alluvium, we felt it was premature to specify layering in the alluvium. We used a shear-wave velocity of 600 m/sec in the alluvium. This is similar to the average shear-wave velocity found by Joyner *et al.* (1981) for alluvium in the southern portion of the Santa Clara Valley. Velocity logging of a shallow borehole just north of the study area found a slower shear-wave velocity in the top 100 feet of the alluvium (Joyner *et al.*, 1976). Using a lower velocity, however, would reduce the accuracy of the
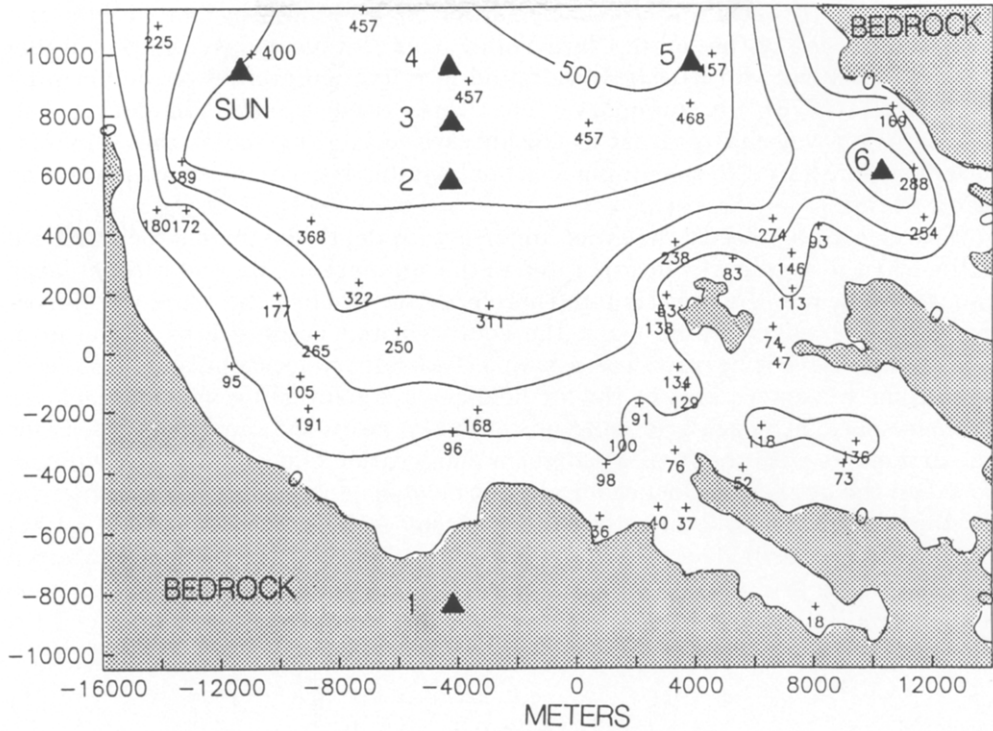
FIG. 3. Model of Santa Clara valley used in the 3-D simulation. Area corresponds to box in Figure 1. Contours represent depth of alluvium derived from fit to water well data and assigned depth points. Contour interval is 100 m. Shading indicates areas where bedrock is at the surface. Most of the crosses in the basin indicate locations of water wells, with depth to bedrock given in meters (from California Department of Water Resources, 1967). Cross with 400-m depth near SUN and 457-m depths in the center of the valley have postulated depths and are not from water well information (see text). Triangles show locations used for the synthetic seismograms shown in Figures 7, 8, 9, and 10. SUN denotes location of the Sunnyvale dense array. Line with zero depth is the alluvium-bedrock surface contact.

finite-difference method for a given frequency. Reflectivity synthetics derived from plane-layered model show that adding a 100-m-thick layer with very low velocity (300 m/sec) on the top of the 600 m/sec alluvium can significantly increase the duration of motion. This implies that the finite-difference synthetics may underestimate the duration of shaking because of the relatively high shear-wave velocity chosen for the alluvium in the model.

We chose a P-wave velocity of 1.1 km/sec for the alluvium. This is lower than the P-wave velocity of 1.8 km/sec for the alluvium found in refraction surveys to the north of the study area (Hazelwood, 1976). Using this larger value of V_P in the simulation caused an instability in the free-surface boundary condition (see also Vidale and Clayton, 1986). The difference between V_P in the model and the measured value will alter somewhat the dispersion curve of the Rayleigh waves. For a plane-layered model with alluvial thickness of 400 m, we found that the group velocity of the Airy phase of the fundamental Rayleigh wave changes from 0.22 km/sec to 0.30 km/sec for V_p of 1.1 and 1.8 km/sec, respectively (see below).

We used a P-wave velocity of 3.5 km/sec and an S-wave velocity of 2.0 km/sec for the bedrock. These velocities are similar to those found by Joyner *et*

al. (1981) for Franciscan rock at the base of a 180-m-deep borehole in the southern portion of the Santa Clara Valley. Our *P*-wave velocity is comparable to the 4.0 km/sec value for bedrock found in refraction profiles to the north by Hazlewood (1976). In summary, the model used in our simulation had a shear-wave velocity contrast of 0.6 km/sec to 2.0 km/sec at the alluvium-basement interface. No smoothing was applied; this transition occurred over one grid spacing.

We assigned a velocity that was uniform with depth for the bedrock because of the way the source was incorporated in the simulation. The grid was not large enough to include the hypocenter. Therefore, we specified the source by imposing synthetic seismograms along the southern and bottom faces of the grid. Each synthetic seismogram was a simple two-sided velocity pulse whose peak amplitude was determined by the far-field *S*-wave solution for an earthquake in a whole-space. For each grid point on these two faces, the radiation pattern for an earthquake with the focal mechanism and location of event 1 was calculated, based on the angle of incidence for a uniform whole-space. The focal mechanism for this earthquake was mainly thrust (strike = 125°, dip = 25°, rake = 100°; Oppenheimer, 1990). The peak amplitude of each velocity seismogram inserted into the whole grid was specified so that its corresponding displacement pulse had an area Ω_0 equal to

$$\Omega_0 = \frac{M_0 R_{\theta\phi}}{4\pi(\beta_r \rho_r \rho_s)^{1/2} \beta_s^{5/2} R}.$$ (1)

Here M_0 is seismic moment, $R_{\theta\phi}$ denotes radiation pattern coefficient, R is distance between grid point and hypocenter, β is *S*-wave velocity, and ρ represents density. The *s* and *r* subscripts denote values taken at the source depth and at the receiver, respectively. In our case, the receivers are located along the southern and bottom sides of the grid, in bedrock. Equation (1) is taken from Aki and Richards (1980) and accounts for the amplitude difference produced by the impedance contrast between the source velocity and the receiver velocity. We used $\beta_r = 2.0$ km/sec, $\beta_s = 3.4$ km/sec, and $\rho_r = \rho_s = 2.6$ gm/cc. The shear-wave velocity at the source depth (10.2 km) for event 1 was estimated from a *P*-wave velocity model found by Dietz and Ellsworth (1990).

The moment for event 1 was determined from *S*-wave displacement spectra derived from recordings of GEOS instruments at sites KOI and DMD (see Mueller and Glassmoyer, 1990). These stations are located at hypocentral distances of 11 and 23 km, respectively. Long-period spectral levels Ω_0 were estimated from both horizontal components and summed vectorially. The moment was calculated from

$$M_0 = \frac{4\pi(\beta_r \rho_r \rho_s)^{1/2} \beta_s^{5/2} R \Omega_0}{F R_{\theta\phi}},$$

where F is the free-surface correction, here taken to be 2. For the moment calculation, we used an average radiation pattern coefficient of 0.67 (Boore and Boatwright, 1984) and a shear-wave velocity at the receiver of 2.0 km/sec. β_s was set equal to 3.4 km/sec, as above. Based on these values, we found a moment of 5.2×10^{22} dyne cm for event 1. This moment was used in equation

(1) to specify the amplitudes of the synthetics inserted into the finite-difference grid.

SNAPSHOTS AND SYNTHETICS FROM 3-D SIMULATION

Figure 4 depicts color snapshots of the east–west component of velocity for two times in the 3-D simulation. Both a map view and a vertical cross section are shown for each time. The cross section is for a north–south slice located 12 km from the western edge of the simulation, through the portion of the basin with the greatest north–south extent in the grid. Both the map view and the cross sections show the contact between the alluvium of the basin and the rock around and beneath the basin. The snapshot for 5 sec after the start of the simulation (Fig. 4, *top*) displays the initial *S*-wave pulse that was input along the southern and bottom faces of the grid. This is a two-sided pulse with westward motion (green) followed by eastward motion (dark blue) with equal amplitude and duration. The input pulse has a period of 1.6 sec. Note the node in the radiation pattern near the eastern side of the grid. There is some motion out ahead of the *S* wave traveling westward in the lower left part of the grid. This appears to be *S*-to-*P* wave conversions from the southern border of the basin. Minor motions are observed out in front of the *S* wave in the basin, which are *S*-to-*P* conversions from the bottom of the basin. Because the source is located well to the south of the grid, most of the input *S*-wave energy on the east–west component consists of *SH* waves.

The snapshot for 11 sec (Fig. 4, *bottom*) illustrates seismic energy reverberating in the basin. We see several east–west-trending wavefronts south of the initial *S* wave. The northernmost dark blue band is wider than the initial green wavefront because it contains the blue wavefront from the backswing of the initial *S* wave followed immediately by the blue band from the *S* wave that was first reflected by the free surface and then reflected by the alluvium-rock interface. Each reflection at the alluvium-rock interface produces a polarity reversal. The basin reverberations are confined to areas of the basin 100 m or greater in thickness. These are areas where the basin is at least two grid points thick (counting the free-surface grid point). The wavefronts curve around the Oak Hill area and are generally parallel to the contour lines of basin depth (compare with Fig. 3). Trapped energy can also be observed in the subbasin just to the north of the Santa Teresa Hills (see Fig. 1 for place names). In the vertical cross section for 11 sec (Fig. 4, *bottom left*), the free-surface reflection of the initial *S* wave forms the right side of the inverted V shape in the northern part of the panel. Energy from multiple reflections within the alluvium leaks out into the rock, as shown by the tails extending below the alluvium in the cross section.

The time slice at 11 sec (Fig. 4, *bottom*) displays the beginning of a Love wave produced along the southern portion of the basin. This is the narrow red band near the middle of the map view. Successive *S*-wave reflections within the southern portion of the basin have decreasing phase velocities because of the northward dip of the alluvium-bedrock interface. Eventually, the multiple reflections are critically trapped within the alluvium, producing Love waves. The Love waves have shorter periods with decreasing phase velocity, producing a dispersed wavetrain with long-period waves followed by a large, short-period Airy phase, This Airy phase can be identified by its slow group velocity in the time slices and in the synthetics that will be discussed later. The Airy phase of
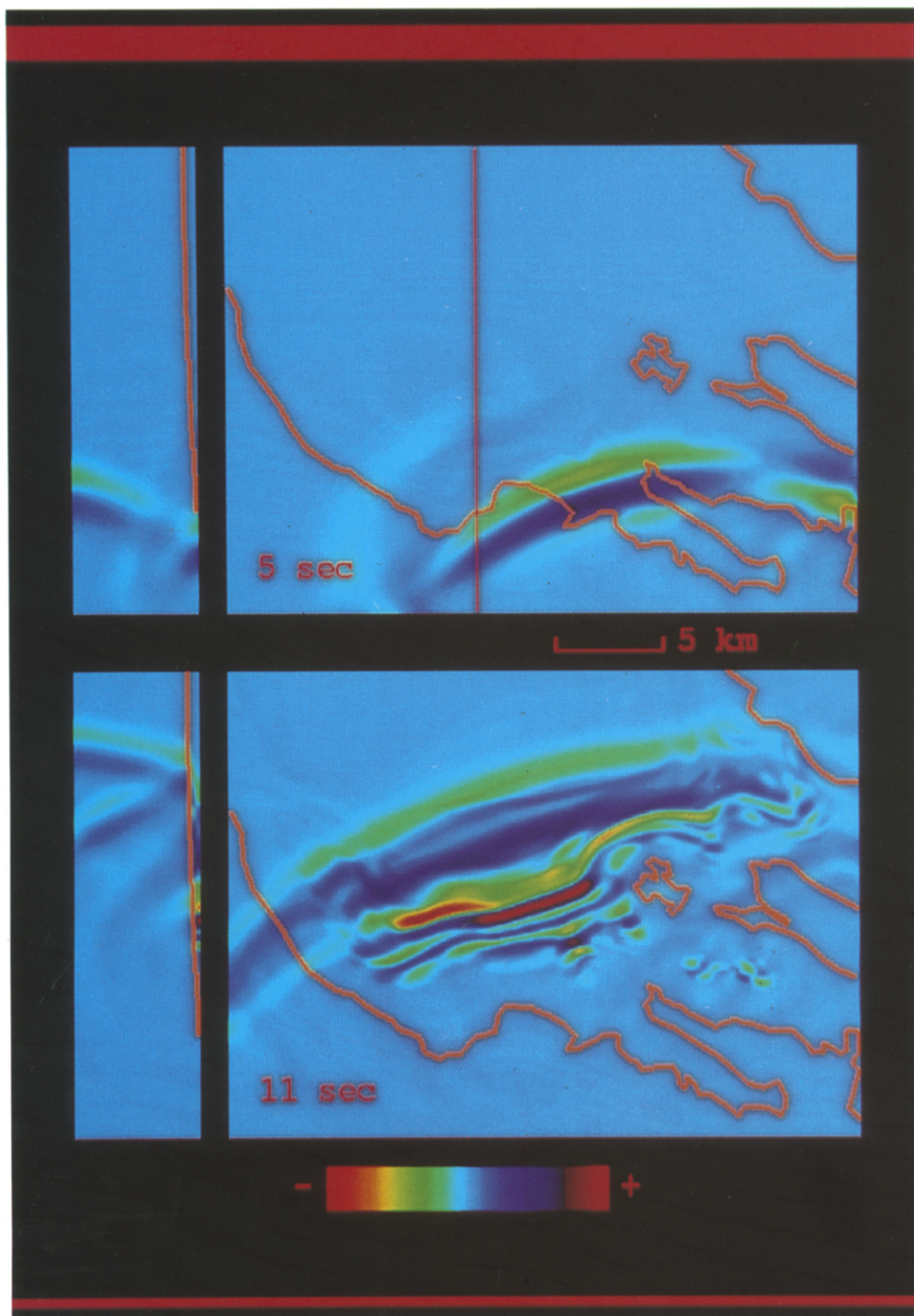
FIG. 4. Snapshots (or time slices) of the east–west component of velocity from the simulation of event 1, showing a map view (*right*: 30 by 22 km) and vertical cross section (*left*; 22 by 6 km in depth) for each time step. Colors are keyed to the amplitude of the ground velocity based on the palette shown at the *bottom*. Positive motion is eastward; negative motion is westward. Maximum velocity is 0.25 cm/sec. The cross sections are for a north–south slice at the vertical line shown in the map view (*top*), intersecting the locations of stations 1 to 4 shown in Figure 3. Depth increases to the left on the cross sections. Alluvium-rock contact is shown by yellow outline in map views and cross sections.

the Love wave contains the largest amplitude in the simulation for the east–west component and comprises the red band in the time slices. Note how the separation between the wavefronts decreases from north to south in the snapshot, exhibiting normal dispersion. This pattern is maintained as the wavefronts propagate northward.

By 17 sec into the simulation (Fig. 5, *top*), the initial S-wave pulse has propagated out of the grid to the north. Now the energy in the basin consists of multiple body-wave reflections and surface waves. The Airy phase of the Love wave (red area) has propagated further to the north at a much slower speed than the initial S wave and its multiple reflections. As before, this Love wave forms the largest amplitude on the east–west component. The vertical cross section shows that the energy in the southern part of the basin is trapped within the alluvium. The northernmost green wavefront has energy extending southward below the alluvium, indicating that it is precritically reflected at the alluvium-rock interface.

At 23 sec into the simulation (Fig. 5, *bottom*), the wavefronts are more segmented in space and the wave field in the basin is even more complex than before. The Airy phase of the Love wave (red band in the upper middle of the map view) is, as before, the largest motion in the snapshot. We also see north–south-trending wavefronts in the northeastern part of the basin. This is surface-wave energy that has been produced along the steep northeast edge of the basin by conversion of incident S waves and scattering of Rayleigh waves traveling northward in the eastern part of the basin (see below). The scattered surface-wave energy is traveling westward across the basin and, since it is radially polarized, consists of Rayleigh waves. We will return to these significant arrivals later in the paper.

Snapshots of the north–south motions for 12 and 16 sec after the start of the simulation are shown in Figure 6. At 12 sec, the initial S wave is near the north end of the grid (Fig. 6, *top*). There are several bands following the initial wavefront, consisting of body waves multiply reflected in the alluvium. The bright yellow-green band just north of Oak Hill is a Rayleigh wave. As the S wave multiply reflects within the alluvium, its phase velocity decreases because of the northward dip of the alluvium-bedrock interface. Eventually, the body waves become more critically reflected and form Rayleigh waves within the alluvium. We will show later that the Rayleigh waves manifested in the north–south motions are probably the first higher-mode Rayleigh waves. Note that the north–south amplitudes increase to the east in the time slices in Figure 6. This is caused by the radiation pattern of the earthquake.

The snapshot of north–south motion at 16 sec (Fig. 6, *bottom*) contains the largest horizontal motion observed in the simulation (0.34 cm/sec). These large motions occur along the northeast margin of the valley and show up as the red areas. The Rayleigh wave produced in the basin impinges on the edge of the basin and increases in amplitude. This indicates that large amplitudes can occur when surface waves within the valley encounter the far-edges of the basin. Scattering of the Rayleigh wave at the northeast margin of the basin produces much of the westward propagating Rayleigh waves observed in the time slice for the east–west motion at 23 sec (Fig. 5, bottom). Another notable feature of Figure 6 is the energy scattered from Oak Hill that propagates to the northwest. The wavefronts for this scattered energy are oriented roughly north–south.
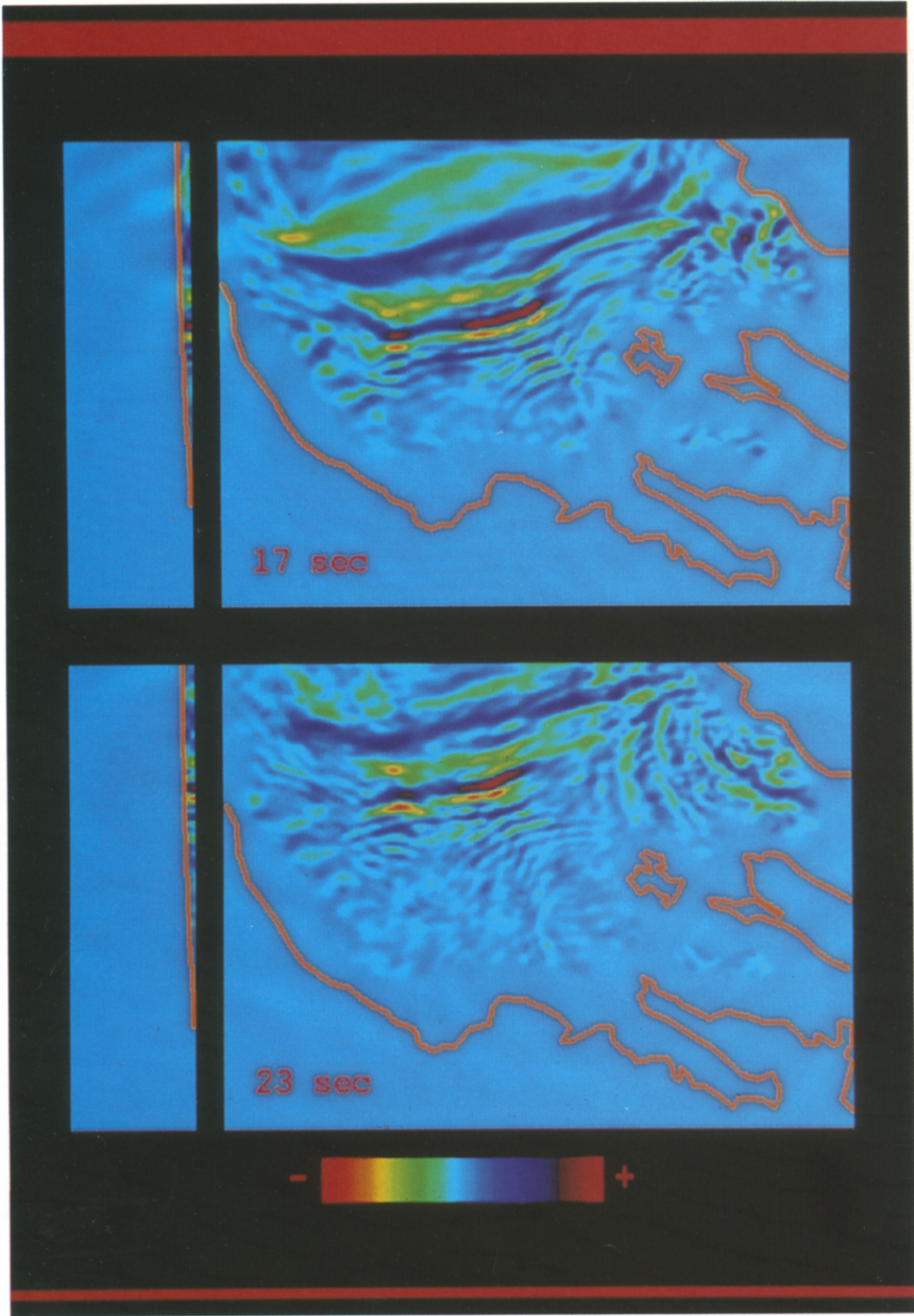
FIG. 5. Snapshots of the east–west component of velocity at (*top*) 17 and (*bottom*) 23 sec after start of simulation. See caption for Figure 4.
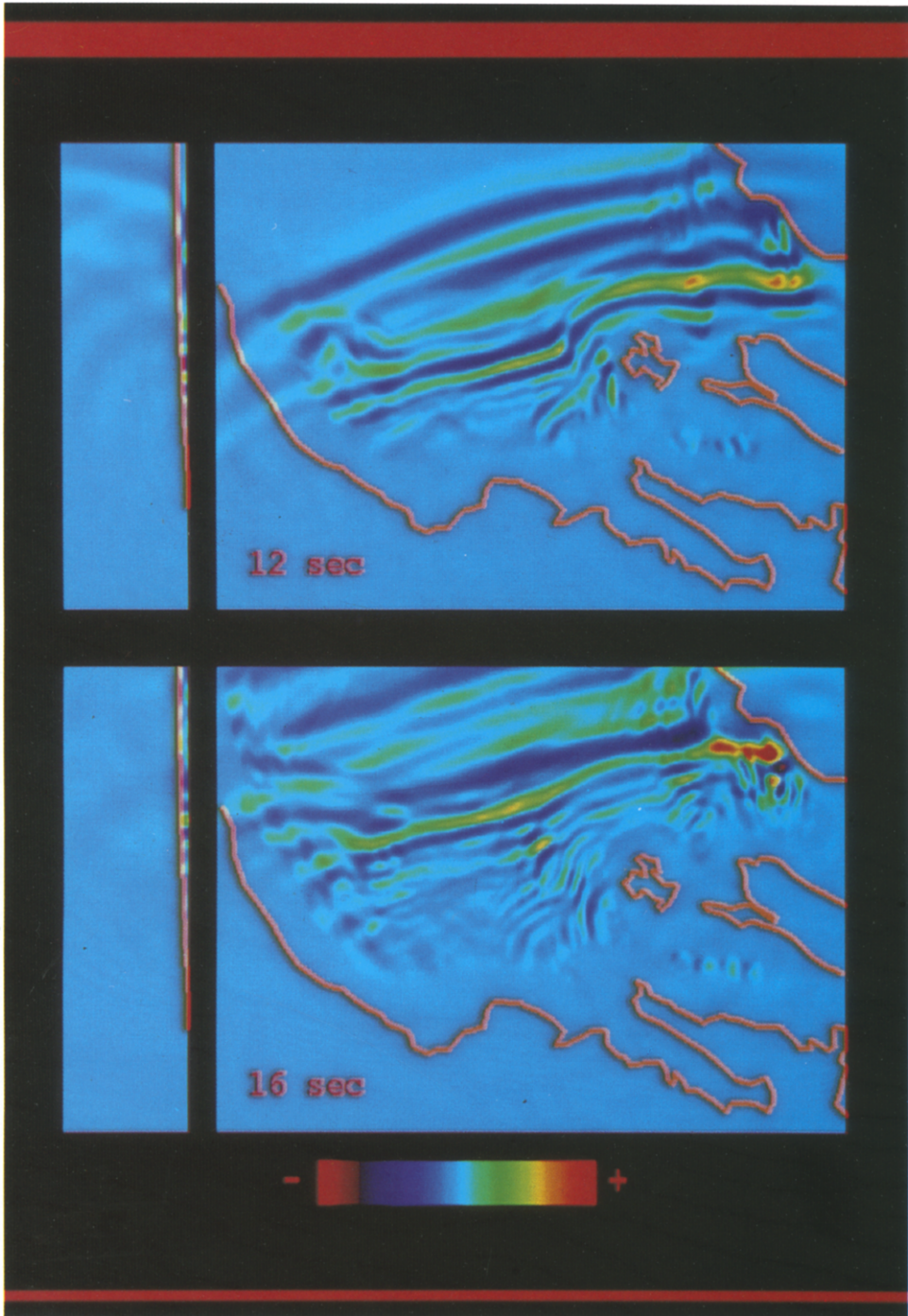
FIG. 6. Snapshots of the north–south component of velocity at (*top*) 12 and (*bottom*) 16 sec. See caption for Figure 4 for details. Maximum amplitude is 0.34 cm/sec. Positive motion is northward.

Figure 7 exhibits synthetic seismograms (velocity) for four surface sites on a north–south line (see Fig. 3 for locations). Site 1 is located on bedrock and the other sites are in the basin on alluvium. East–west, north–south, and vertical synthetics are plotted with the same amplitude scale. The east–west and north–south synthetics approximately represent the transverse and radial components of motion, respectively. The synthetics document the large amplitude and prolonged duration of shaking for basin sites compared to rock sites. The initial S-wave pulse is about twice as large at the basin sites than the rock site, for the east–west component. The north–south and vertical components have similar initial S-wave amplitudes at the rock and basin locations.

The Airy phase of the Love wave produced near the southern edge of the basin is clearly seen on the east–west synthetics for the basin receivers and represents the largest amplitude in the east–west synthetics. At the northernmost receiver (site 4), the Airy phase of the Love wave trails the S wave by 18 sec. The arrival time of the Airy phase controls the overall duration of significant ground motions on the east–west synthetics. Thus, stations near the center of the basin have longer durations of motion than basin sites near the border of the valley.
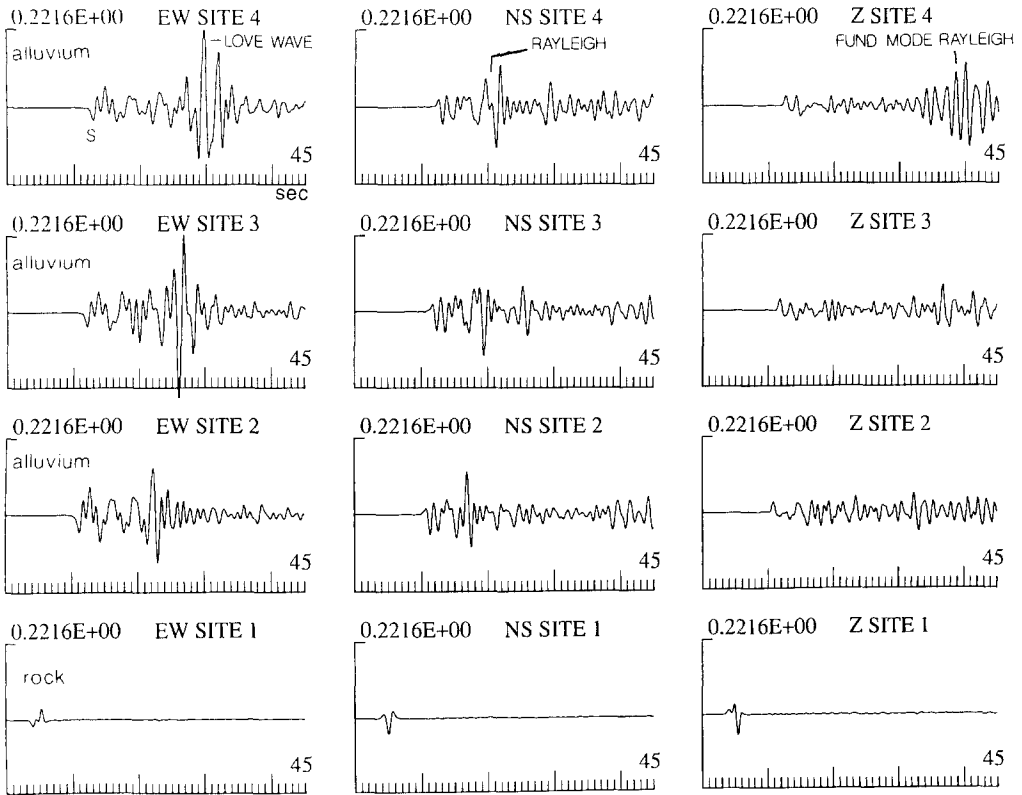

FIG. 7. East–west, north–south, and vertical velocity synthetics from the 3-D simulations for sites 1 to 4 (see Fig. 3). Numbers above each panel indicate peak amplitudes in cm/sec. All panels are scaled to the same amplitude. Note the small amplitude and short duration of the waveform at the rock site (no. 1), compared to the basin sites (no. 2 to 4). Note the Love wave on the east–west component that forms the largest amplitude in the records and is increasingly delayed with respect to the initial S wave as the epicentral distance increases.

We compared the group velocities of the Love and Rayleigh waves observed in the simulations with those predicted using a flat layered model for the basin. We used an alluvium thickness of 400 m. Alluvium and bedrock velocities were the same as used in the simulations. Phase and group velocities and eigenfunctions for Love and Rayleigh waves were computed using the method of Saito (1967). Figure 8 shows the dispersion curves calculated for this model, for Love waves and fundamental-mode and first higher-mode Rayleigh waves. We found that the flat-layered model produces a Love-wave Airy phase at a period of 2.5 sec with a group velocity of 0.41 km/sec. We measured a group velocity of about 0.5 km/sec from the synthesis in Figure 7 for the portion of the Love wave with the largest amplitude, consistent with the group velocity for the flat-layered model. Thus, the east–west synthetics are characterized by a dispersed Love wavetrain with short-period energy following longer-period energy and culminating in an Airy phase.

Of course, anelastic attenuation will reduce the amplitude of the Love wave as it propagates in the basin. Using a shear-wave Q of 20 for the alluvium, a travel time of 10 sec, and a period of 2 sec reduces the amplitude by a factor of 0.46. The Love wave would still be comparable in amplitude to the direct S wave. Even with low Q values in the alluvium, the Love wave substantially increases the duration of shaking for basin sites.

Surface waves are also observed on the north–south and vertical synthesis (Fig. 7). A long-period phase arrives 4 to 7 sec after the S wave on the north–south component at the basin sites. This is the arrival seen as the bright yellow-green band in the time slices in Figure 6 and comprises the peak amplitude on the north–south synthetics (Fig. 7). At site 4 this arrival appears to be dispersed with longer-period energy preceding shorter-period energy. We estimate the group velocity of this arrival at about 1.0 km/sec, based on the synthetics in Figure 7. This arrival is probably a mixture of fundamental- and first higher-mode Rayleigh waves, based on comparison with dispersion curves and eigenfunctions calculated for a flat-layered model. Both types of Rayleigh waves have similar group velocities to the synthetic arrivals and, for these periods, have larger theoretical amplitudes on the radial component than on the vertical component, also in agreement with the synthetics. The flat-layered model of the basin predicts a level portion of the group velocity curve for the first higher Rayleigh wave mode at periods between 1.0 and 1.5 sec with a group velocity about 0.9 km/sec (see Fig. 8), comparable to that found in the synthet-
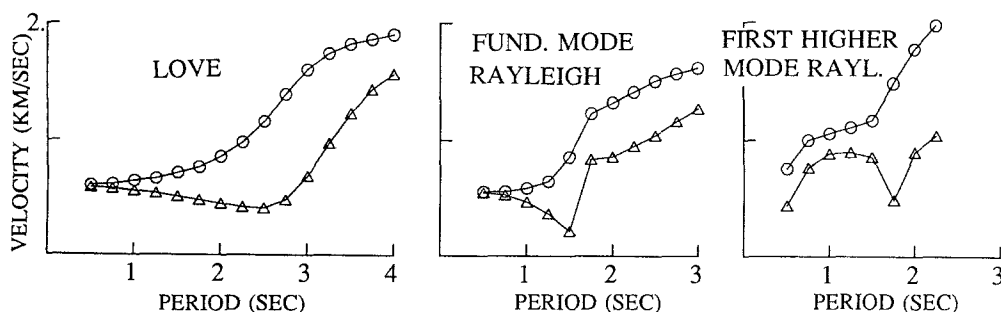

FIG. 8. Theoretical dispersion curves for a 400-m-thick alluvium layer above a half-space (see text). Circles denote phase velocities; triangles are group velocities.

ics. The eigenfunctions calculated for this higher mode Rayleigh wave indicate that its amplitude should be about 3 times larger on the radial component than the vertical component, at these periods. This may explain why the Rayleigh wave is observed mainly on the north–south synthetics and is not prominent on the vertical synthetics (Fig. 7). The fundamental-mode Rayleigh wave also has a group velocity of about 1.0 km/sec for periods between 1.75 and 2.5 sec (Fig. 8). For these periods the fundamental-mode Rayleigh wave has a predicted amplitude on the radial component between 4 and 6 times that on the vertical component. We will show later that the phase velocity of this arrival found from the synthetics is consistent with either the fundamental- or higher-mode Rayleigh waves. We conclude that the largest arrival on the north–south synthetics is a Rayleigh wave. This Rayleigh wave is generated by conversion of the incident S wave along the southern margin of the valley.

The vertical synthetic for station 4 exhibits a sizable Rayleigh wave near the end of the record. It is difficult to estimate the group velocity of this arrival, since it is only distinct at site 4. The late arrival time indicates that it has very slow group velocity, much less than 0.5 km/sec measured for the Love wave. The flat-layered model predicts the Airy phase for the fundamental-mode Rayleigh wave to have a period of 1.5 sec and a very slow group velocity of 0.22 km/sec (see Fig. 8). Furthermore, the Airy phase in the flat-layered model should be 2.1 times larger on the vertical component than the radial, based on its eigenfunctions. This is consistent with the synthetics, where this arrival is seen clearly on the vertical component at site 4, but not on the north–south component. We conclude that this late arrival is a fundamental-mode Rayleigh wave in the alluvium, produced by conversion of the incident S wave. Analysis of arrival times of synthetics at points adjacent to site 4 indicates that this arrival is propagating to the north and is not a reflection from the northern edge of the grid. This Rayleigh wave is not seen distinctly at sites 2 and 3, implying that it may require a flat portion of the alluvium-bedrock interface to develop.

In Figure 9, we compare the synthetic seismograms with observed displacements for event 1 from station SUNC of the Sunnyvale dense array. Both the synthetics and the observed data are rotated to the transverse and radial components and are low-pass filtered with a corner at 1 Hz. A high-pass filter with a corner at 0.04 Hz was applied to the synthetics to remove a step-like artifact in the displacement seismograms. A Q operator that changes with time in the record was convolved with the synthetics to approximate the effect of anelastic attenuation on the waveforms (see Vidale and Helmberger, 1988). A different Q operator was applied to each 1.5-sec window of the synthetics. Letting t denote time in the record, the t^* for this operator was calculated from

$$t^* = t_s^* + \frac{t - t_s}{Q}.$$

Here t_s is the arrival time of the direct S wave in the synthetic and Q is the value for alluvium. Note that $t_s^* = \int Q^{-1} \, dt$, where the integral is taken over the S-wave travel time from source to receiver. This procedure assumes that energy arriving at t sec in the seismogram has traveled $t - t_s$ sec in the alluvium. This method does not use separate P- and S-wave Q values. The Q used here corresponds to the shear-wave Q in the alluvium, since the attenua-

tion of surface waves (Love and Rayleigh) trapped in the alluvium is controlled by this shear-wave Q.

The synthetics in Figure 9 were derived using a t_s^* of 0.03 and Q of 50 in the alluvium. This relatively high Q for alluvium was chosen so that later-arriving Rayleigh waves wouldn't be completely removed, in keeping with observations of late arrivals from the Sunnyvale dense array (see below).

The synthetics for the dense array site SUN (*middle row* in Fig. 9) have similarities and differences with the observed seismograms. The transverse synthetics contain a long-period Love wave after the S wave, analogous to the long-period Love wave observed in the actual records. However, the Love wave in the synthetics arrives only 8 sec after the initial S wave (*middle left panel* in Fig. 9), whereas the largest part of the observed Love wave arrives 17 sec after the initial S wave (*top left panel* in Fig. 9; see also Frankel *et al.*, 1991). The transverse synthetics underestimate the duration of ground motions. This discrepancy may be caused by using a shear-wave velocity in the alluvium that is too fast or by underestimating the thickness of the alluvium south of SUN. Frankel *et al.* (1991) demonstrated that a flat-layered structure could not produce the observed Love waves. While the simulation does not duplicate the timing of these arrivals, it does demonstrate that the observed Love waves were likely produced by conversion of the incident S wave near the southern margins of the valley.

The radial synthetics at SUN have a duration similar to the observed radial records. The long-period Rayleigh wave arriving about 2 sec after the S wave in the observed seismogram is present at a similar time in the synthetic. This is the first higher-mode Rayleigh wave described above, produced by conversion of the incoming S wave. There is little correspondence between the vertical
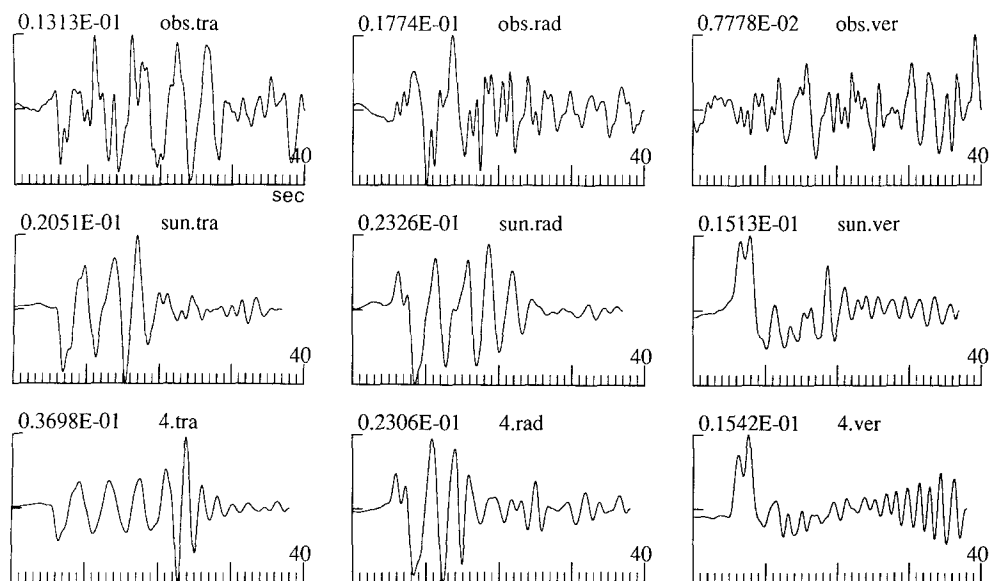

FIG. 9. Comparison of displacement seismograms observed at the Sunnyvale dense array (*top row*, station SUNC) and synthetic seismograms for that location (*middle row*, "sun") and at site 4 (see Fig. 3). Transverse (*left column*), radial (*middle column*), and vertical (*right column*) components are shown. Number above each seismogram is the peak displacement in cm. These seismograms have been processed with a Q operator that varies with time in the record.

synthetic and observed seismogram. The direct S-wave arrival is very promi-
nent in the vertical synthetic, but not in the observed record. This could be due
to overestimating the shear-wave velocity in the near-surface. Using a slower
S-wave velocity would cause the S wave to be more steeply incident at the
surface, reducing its amplitude on the vertical component.

The peak amplitudes of the synthetics at SUN are comparable to the observed
peak amplitudes, for the transverse and radial components. The peak displace-
ments on the transverse and radial synthetics are 1.6 and 1.3 times the
observed transverse and radial amplitudes, respectively. Considering the sim-
plistic velocity model used in the simulations, the similarity of the observed and
peak amplitudes is encouraging.

To gain insight on how differences in site location affect the synthetic seismo-
grams, we show in Figure 9 (bottom row) displacement synthetics for station 4,
located about 7 km east of SUN. These seismograms were processed with the
same time-varying Q operator as the synthetics for SUN. For site 4, the Love
waves have a longer travel path in the basin, compared to SUN. The Love wave
on the transverse component is delayed more than for the synthetic at SUN and
the overall duration of large motions is similar to the observed transverse
record for the dense array. Thus, if we had thickened the alluvium in our model
south of SUN or made it lower velocity, we could have delayed the arrival of
Love wave on the SUN synthetics so that their arrival time matched the
observed records. Our knoweldge of the structure of the basin is not sufficient,
at this time, to accurately predict the duration of transverse motion for basin
sites.

Another notable feature of the synthetics for site 4 is the fundamental-mode
Rayleigh wave on the vertical component (Fig. 9, bottom right). As mentioned
above, this Rayleigh wave was converted from the S wave incident along the
southern margin of the basin. There are some late, long-period arrivals on the
observed vertical record (Fig. 9, top right) that may respond to such a S-to-
Rayleigh-wave conversion. If we had used values of Q much smaller than 50,
this Rayleigh wave would have insignificant amplitude in the synthetic. The
presence of such late arrivals in the observed seismograms may place a lower
limit on the effective Q for Rayleigh waves in the alluvium.

Figure 10 shows synthetic seismograms for stations along an east–west line
across the valley, along with station 6 located within the eastern portion of the
valley. These are the original velocity synthetics and do not incorporate anelas-
tic attenuation. The east–west synthetics have longer duration of shaking and
larger peak amplitudes for site 4 in the center of the valley than for the other
sites closer to the edges of the basin. In contrast, the north–south motions have
about the same duration regardless of the position of the station within the
valley. Both the north–south and vertical motions are relatively large for site 6
in the eastern part of the valley. This site is located within a part of the basin
model that has a depth of 300 m, with shallower depths surrounding it. Some of
this may be due to radiation pattern, but much of the amplitude difference must
be caused by propagation effects within this enclosed, deeper part of the basin,
such as focusing or resonance.

ARRAY ANALYSIS OF SYNTHETICS

We saved the synthetic seismograms for closely spaced receivers so that we
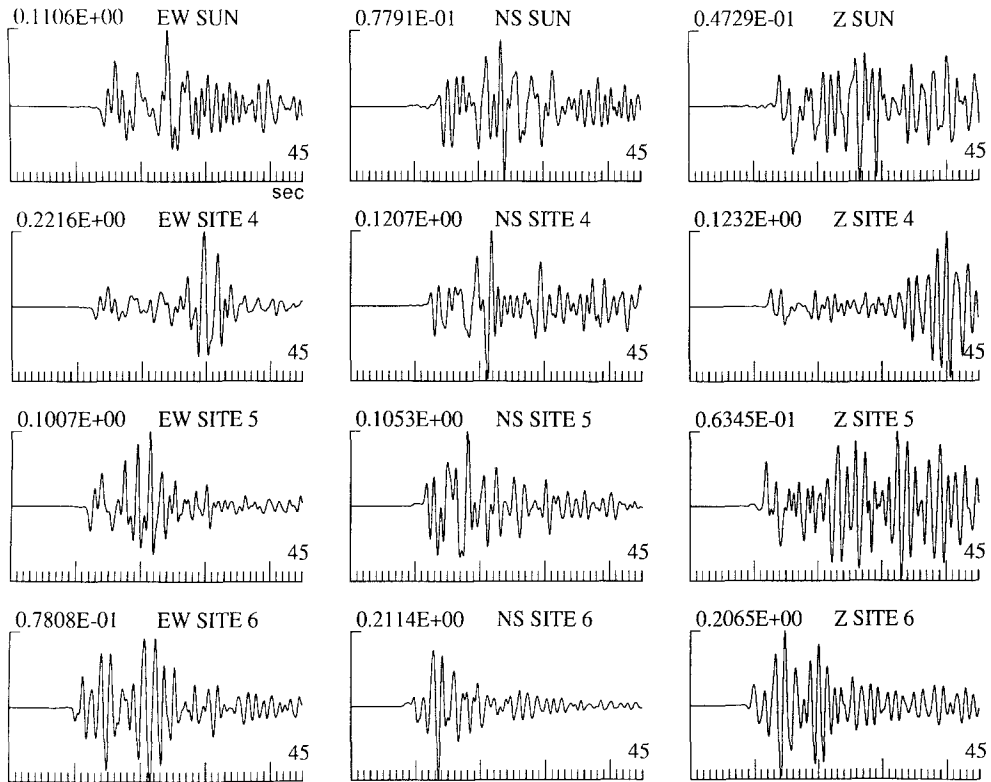could use array analysis to determine the apparent velocity and direction of

FIG. 10. Synthetic velocity seismograms for stations across valley (see Fig. 3 for locations). Peak amplitudes are given in cm/sec. Anelastic attenuation is not included.

propagation for various arrivals in the synthetics. Three arrays were considered. Each array had nine receivers arranged in a square pattern with three stations on a side. The station spacing in both the north–south and east–west directions was 200 m. We used a cross correlation method for determination of vector slowness that was applied by Frankel *et al.* (1991) to seismograms of Loma Prieta aftershocks recorded by the Sunnyvale dense array. This method finds the maximum cross correlation of waveforms over a range of north–south and east–west slownesses, for a windowed portion of the seismograms. The vector slowness corresponding to the maximum cross correlation represents the slowness of arrivals for that window.

Figure 11a shows the results for the nine synthetic seismograms (east–west component of velocity) of an array around station SUN (see Fig. 3 for location). Only results for windows with cross correlations of 0.8 or greater are shown. A window length of 2 sec was used. The initial S wave has an apparent velocity of 1.7 km/sec and a backazimuth of 153°. This backazimuth is essentially the same as the backazimuth to the epicenter (measured clockwise from north). The apparent velocity is about equal to that expected for the direct S wave, considering propagation across the northward-dipping interface between the alluvium and bedrock. Transmission of the direct S wave across an alluvium-bedrock interface with a 5° northward dip would produce an S wave with an apparent velocity of 1.6 km/sec.

The apparent velocities of arrivals in the synthetics generally decrease with increasing time in the waveform (Fig. 11a). This is qualitatively similar to the results from the Sunnyvale dense array for the four Loma Prieta aftershocks studied in Frankel *et al.* (1991). For times between 20 and 40 sec from the start of the synthetics (Fig. 11a), the apparent velocities are generally between 1.0 and 1.1 km/sec, significantly less than the initial S-wave arrival. The slow apparent velocities signify that these later arrivals are surface waves. Since the east–west component is oriented approximately transverse to the direction of propagation, these surface waves are Love waves. The Love wave comprises the largest phase on the synthetic, at 24 sec after the start. A flat-layered model of the basin predicts a phase velocity of 1.2 km/sec for the Airy phase of the Love
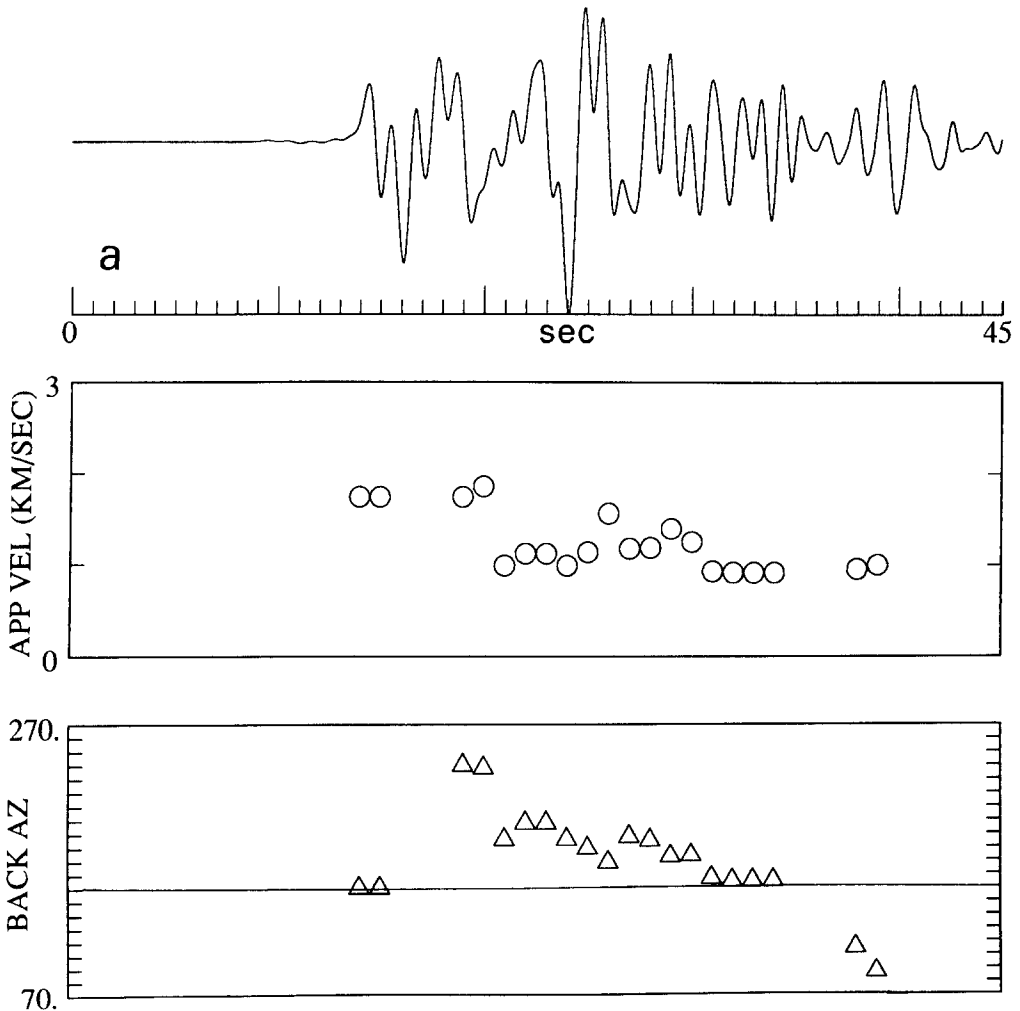

FIG. 11. Results from moving window slowness analysis for synthetics from small-aperture arrays. One of the nine east–west velocity synthetics used in each analysis is shown at the *top*. Backazimuth is measured in degrees clockwise from north. Only measurements with cross correlations ≥ 0.8 are shown. The horizontal line on each backazimuth plot shows the backazimuth to the epicenter. (a) Dense array at SUN (Fig. 3). (b) Dense array at site 4. (c) Dense array at site 5. Note the decrease in apparent velocity with time in the record, indicating the presence of surface waves after the direct S wave. (d) Results from north–south synthetics for array at site 4.
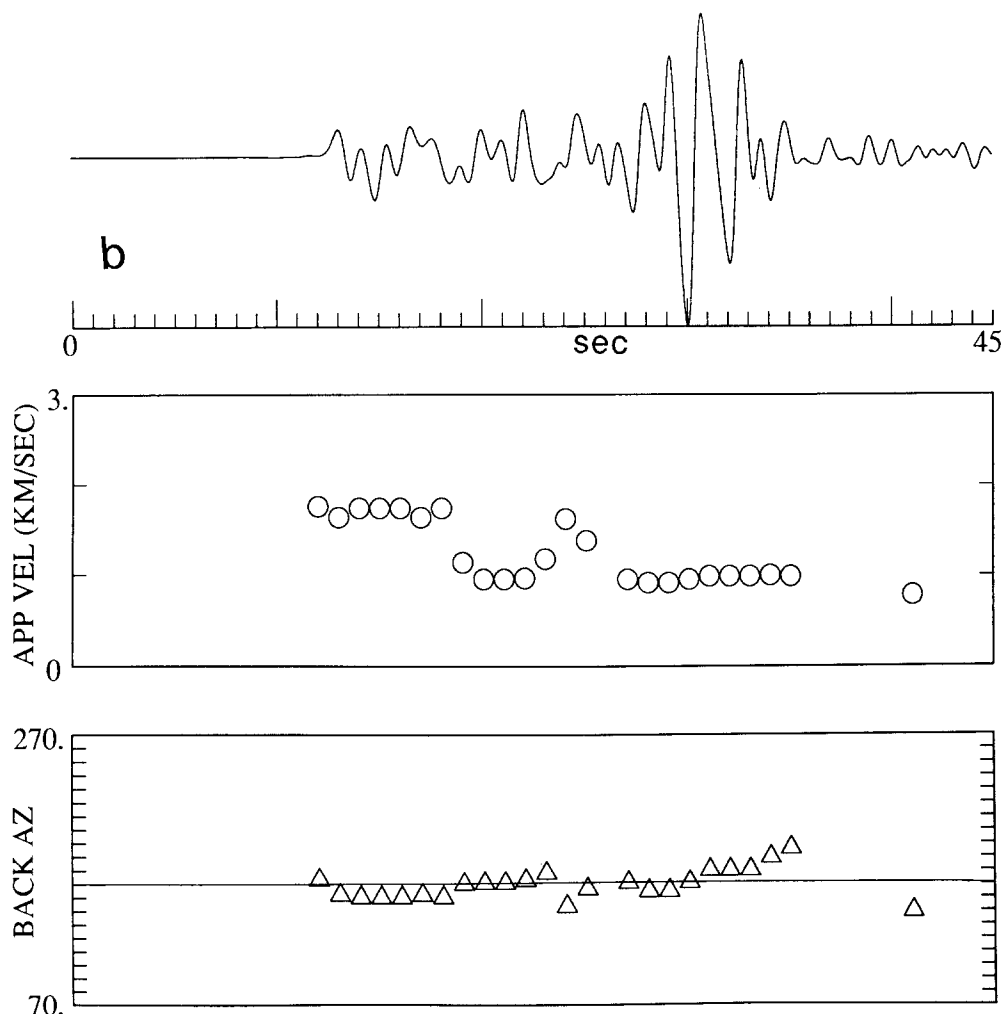
FIG. 11. (*Continued*)

wave, similar to the phase velocity observed in the array analysis. This lends further support to our interpretation of the largest arrival in the east–west synthetics as the Airy phase of the Love wave.

The arrivals between 10 and 25 sec in the record have backazimuths some-what greater than the backazimuth to the source (Fig. 11a). This indicates that these surface waves are coming from a direction more southerly than the source. This is also apparent in the time slices (Figs. 4 and 5), where the surface waves at the western edge of the basin are seen traveling northward, roughly parallel to the western edge of the valley.

Later surface-wave arrivals in the synthetics at SUN are propagating in a westward direction. Figure 11a shows that arrivals 37 to 41 sec into the record have back azimuths of 80° to 110°. These arrivals represent surface waves scattered at the northeastern edge of the valley by incident S waves and Rayleigh waves. These scattered surface waves then travel westward across the valley. The apparent velocity of these arrivals is about 1.0 km/sec, indicating
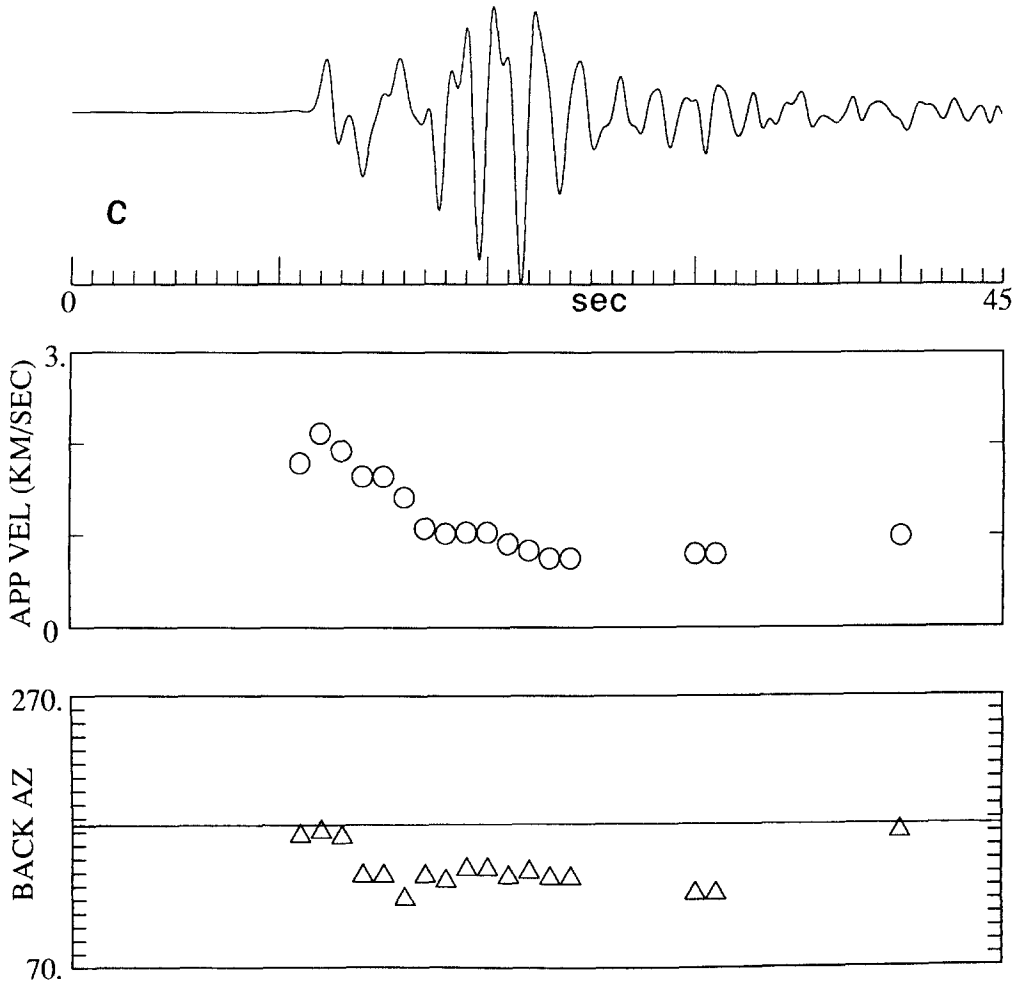
FIG. 11. (*Continued*)

that they are surface waves. Since the east–west component is oriented roughly parallel to the direction of propagation of these arrivals, we conclude that they are Rayleigh waves. These surface waves are apparent in the eastern portion of the valley in the time slice at 23 sec (Fig. 5, *bottom*). Frankel *et al.* (1991) found some surface-wave arrivals traveling in a northwesterly direction across the Sunnyvale dense array in the observed seismograms for aftershock 1. However, these arrivals occurred earlier in the observed seismograms than the synthetics. Westward-propagating surface waves started about 10 sec after the initial S wave in the observed transverse records, whereas they don't arrive until 24 sec after the S wave in the synthetics. Frankel *et al.* (1991) suggested that the westward-propagating arrivals in the observed records may have been scattered from the vicinity of Oak Hill (see Fig. 1). Although the time slices show energy scattered around Oak Hill, some of it in a northwest direction, it is not clear that this energy has significant amplitude by the time it reaches SUN. Certainly, the moving window slowness analysis does not identify this energy. It appears that the large surface waves from the western edge of the basin
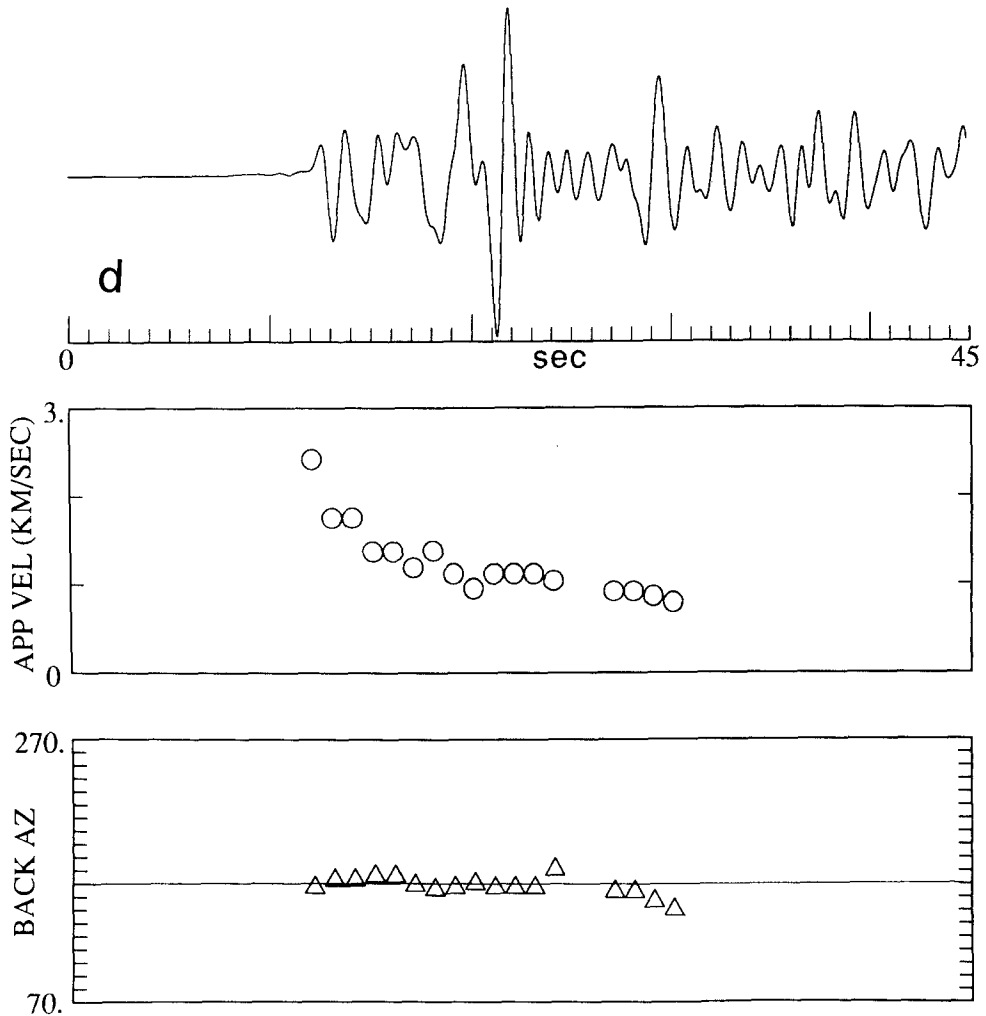
FIG. 11. (*Continued*)

overwhelm the energy scattered from Oak Hill on the synthetics. The observed seismograms for event 1 do not show the late-arriving energy from the eastern side of the basin apparent on the synthetics.

Results of the slowness analysis for an array located around station 4 are depicted in Figure 11b (east–west component). Again, the apparent velocity decreases with increasing time in the synthetics, indicating the transition from direct S wave to multiply reflected S to Love waves. The large arrival at 30 sec into the record has an apparent velocity of 1.0 km/sec and is the Airy phase of the Love wave. Most of the arrivals are coming approximately from the direction of the source.

Figure 11c contains the vector slowness determinations for east–west synthetics from station 5 near the eastern edge of the valley (see Fig. 3). The apparent velocity decreases with increasing time, and a large Love wave arrives at 20 sec into the record with a slow apparent velocity. Most of the arrivals after the initial S wave have backazimuths less than that to the source. This

indicates that these arrivals are traveling parallel to the northeastern edge of the valley and are guided along the long-axis of the subbasin near that edge of the valley (see Fig. 4).

In summary, the largest arrivals in the east–west synthetics consist of Love waves produced by the conversion of incident S waves at the edges of the basin. These arrivals can be identified by their slow group velocity seen in snapshots of the wave field (Figs. 4 and 5) and from synthetics from widely separated receivers (Fig. 7), as well as their slow apparent (phase) velocity found from measurements from arrays in the finite-difference grid (Fig. 11). The arrival of the Airy phase of the Love waves determines the duration of large motions for sites in the basin. Sites near the center of the basin (e.g., site 4) have a longer duration than those near the edges of the basin (sites SUN and 5), because of the increased delay of the Airy phase propagating into the basin (Fig. 10).

We also did array analysis on the north–south synthetics from the array at site 4 (Fig. 11d). The phase velocity is observed to decrease into the record. The largest arrival (21 sec into the record) has a phase velocity of about 1.1 km/sec. Earlier in this paper, we identified this arrival as a Rayleigh wave. This phase velocity is essentially the same as that found for a first higher-mode Rayleigh wave for periods between 1.0 and 1.5 sec, based on a flat-layered model of the basin (Fig. 8). The longer-period energy preceding the largest arrival has a slightly higher phase velocity between 1.2 and 1.4 km/sec (Fig. 11d). This is roughly consistent with the phase velocities for the fundamental Rayleigh wave for periods of 1.75 to 2.5 sec (Fig. 8). The measured phase velocities of the largest phase on the north–south component support our interpretation that it is a Rayleigh wave. Figure 11d also shows that the backazimuth of this arrival is about the same as that to the source.

The finite-difference synthetics and calculations for flat-layered models document that the Love and Rayleigh waves can have different periods than that expected for S waves multiply reflected in the alluvium. For a 400-m-thick layer of alluvium ($\beta = 0.6$ km/sec), we would expect a resonant period of 2.7 sec for multiply reflected S waves with vertical incidence. Here, the resonant period equals $4H/V_S$, where H is the layer thickness and V_S its shear-wave velocity (Haskell, 1960). Figure 9 (*bottom left panel*) shows that the Love wave contains significant amounts of longer-period energy (≈ 4 sec) preceding the Airy phase. The flat-layered basin model predicts that the Airy phase of the fundamental-mode Rayleigh wave will have a period of 1.5 sec (Fig. 8). This is significantly different from the resonant period for a vertically incident S wave. Thus, the frequency content of surface waves must be accounted for in the design of long-period structures located in sedimentary basins.

EFFECTS OF ANGLE OF INCIDENCE AND SHARPNESS OF VELOCITY TRANSITION

To assess how the conversion of S-waves-to-surface waves is affected by angle of incidence, we used a 2-D SH-wave finite-difference code. The 2-D velocity model was a vertical cross section along a north–south slice 12 km from the left side of the grid. The cross sections on the left-side of the time slices in Figure 4 show the geometry of the alluvium-basin interface used in the 2-D model. The grid spacing for the 2-D runs was 100 m, the same as the 3-D simulation. The grid was 220 grid points across and 100 grid points in depth. The source was an isotropic point source situated in the bedrock 4 km south of the southern edge of the basin. Shear-wave velocities in the rock and alluvium were 2.0 and 0.6

km/sec, respectively, as in the 3-D simulation. By varying the depth of the source, we altered the angle of incidence of S waves on the edge of the basin. Source depths of 1, 5, and 9 km were considered. The angles of incidence (measured from the upward vertical) at the southern edge of the basin were 76°, 39°, and 24°, respectively.

Figure 12 shows the SH synthetics for a receiver located in the basin 2 km from the northern end of the grid ($\Delta = 16$ km). The synthetics are qualitatively similar to the east–west synthetics from the 3-D simulation for station 4 (see Fig. 7). The S wave is followed by multiple reflections in the alluvium and then by a large, shorter-period Love wave. As the source depth is increased and the angle of incidence becomes steeper, the Love wave becomes smaller relative to the direct S wave (Fig. 12). We would expect that trapping of Love waves in the basin would be more efficient for shallow angles of incidence. It is important to stress that, even with the steep angle of incidence for the 9-km-deep source, the Love wave is substantial and has greater amplitude then the direct S wave. This demonstrates that S-to-Love-wave conversion at the edge of basins is important even for steeply incident S waves (see also Bard and Bouchon, 1980a).

It is enlightening to compare these synthetics with that from a crustal model with flat layers. The *bottom panel* in Figure 12 depicts the synthetic for the case where the source is at 5-km depth and the alluvium-bedrock interface is horizontal at 400-m depth. The receiver is located at an epicentral distance of 16 km, as in the above examples. Now we see that there is effectively no Love wave produced at this distance for a source at this depth, for flat layers. This synthetic has much less duration of shaking than the cases with the dipping interface. It is the dip of the alluvium-bedrock interface away from the source that produces the Love wave. As the S wave is multiply reflected within the alluvium, its angle of incidence becomes more grazing so that eventually the S wave is critically trapped in the alluvium forming the Love wave.

Another critical question is how the conversion is affected by the sharpness of the transition between the rock and alluvium. To address this, we specified a region of transitional velocity between the alluvium and the rock. First we started with the original model with 0.6 km/sec alluvium and 2.0 km/sec rock. We then added two layers just below the basin and along its southern edge. Each transitional layer was 200-m thick. The layer closest to the basin had a shear-wave velocity of 1.0 km/sec and the next outer layer had a velocity of 1.5 km/sec. Figure 13 shows the synthetic seismograms for both the original, abrupt boundary and the transitional boundary, for a source depth of 5 km. Because of the presence of more layers, the transitional structure produces a more complex seismogram. The Love-wave conversion from the incident S wave is still present with the transitional boundary, exhibiting large amplitudes about 20 sec into the record. This result indicates that S-to-surface-wave conversion is still significant when there is a transitional boundary between the rock and alluvium. Of course, wider transition zones may reduce the amplitude of the conversion, especially if the transition occurs over a distance much greater than a wavelength.

DISCUSSION

The 3-D simulation provides important insights on how seismic waves propagate in a sedimentary basin with a realistically complex geometry. The synthet-
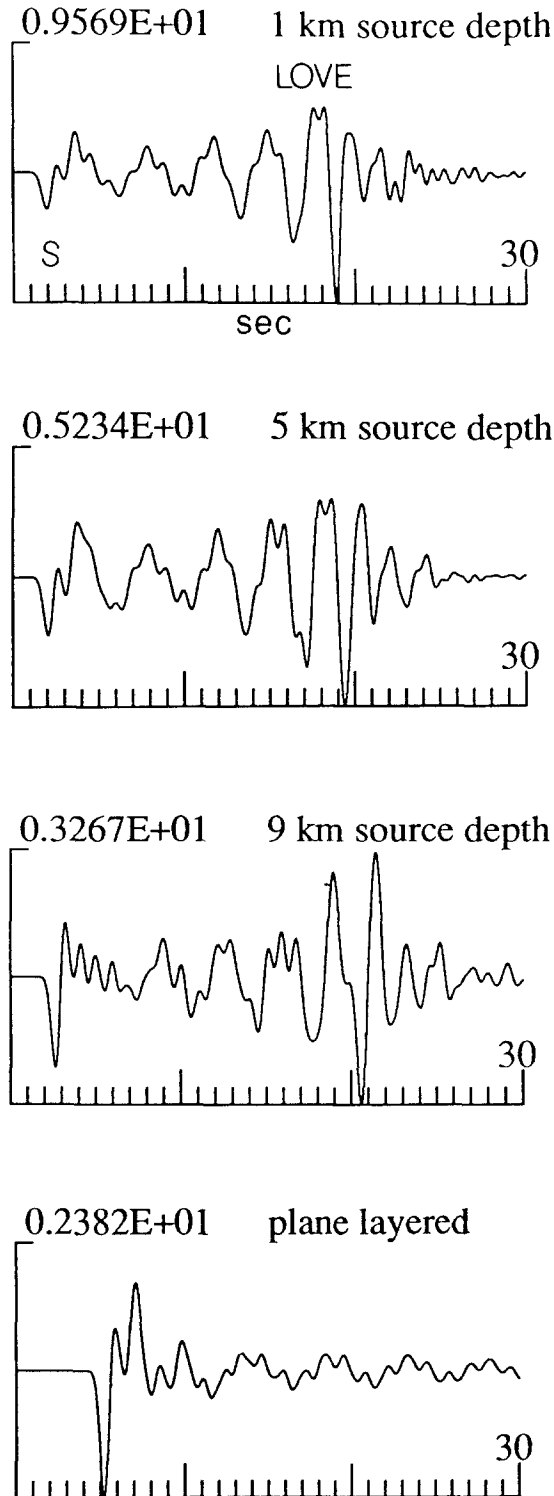
0.9569E+01   1 km source depth

LOVE

S   30

sec

0.5234E+01   5 km source depth

30

0.3267E+01   9 km source depth

30

0.2382E+01   plane layered

30

FIG. 12. *SH* synthetics for a 2-D model of the basin taken from a north–south vertical cross section located 12 km from the western edge of the basin (see Fig. 3). The source is located 4 km south of the southern edge of the basin at depth of 1, 5, and 9 km. Note the large Love wave 18 to 20 sec into the records, for all source depths. *Bottom panel* shows synthetic seismogram for flat alluvium-bedrock interface, 5-km source depth. No Love wave is observed for this case.

0.5234E+01   abrupt
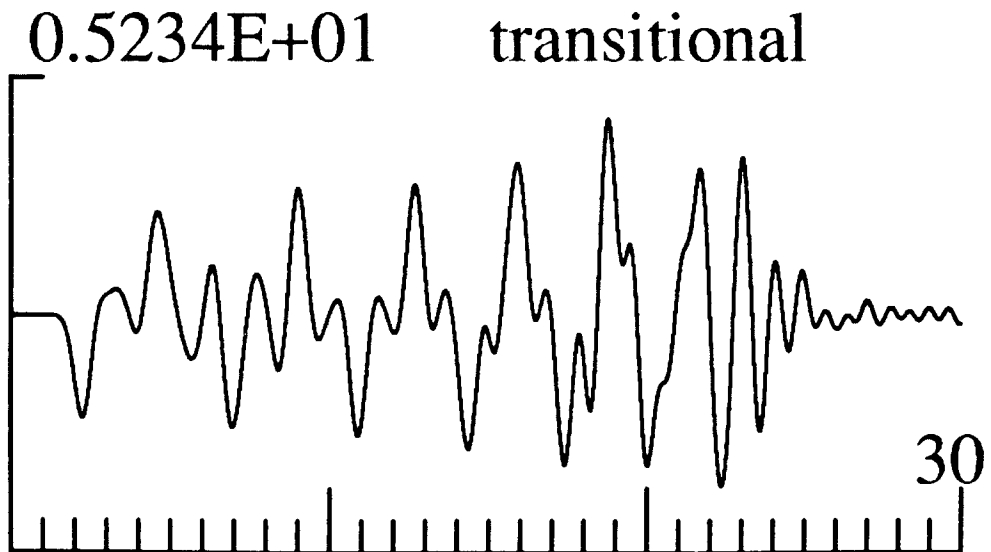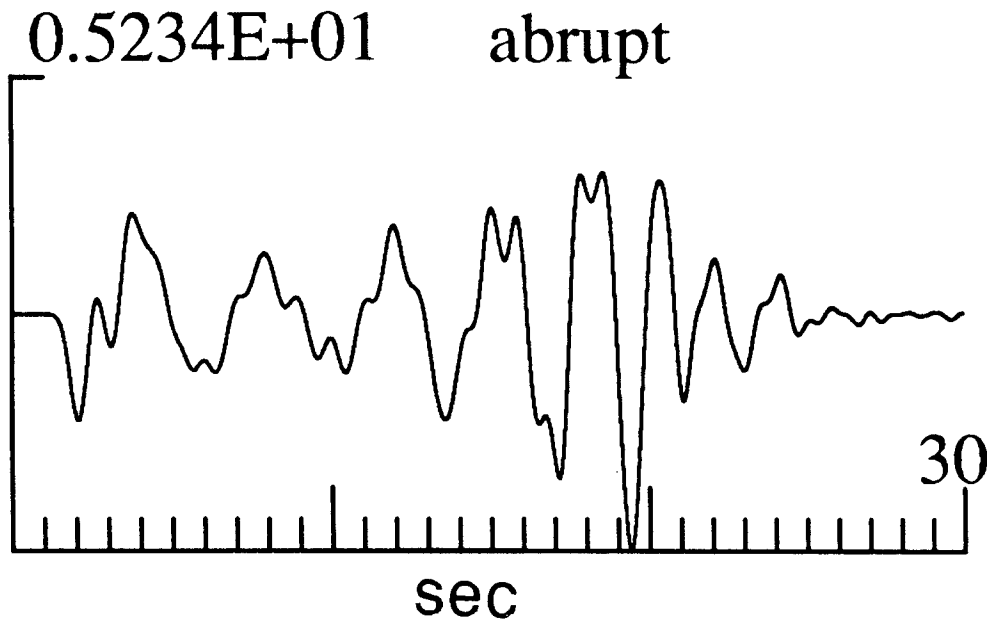

30

sec

0.5234E+01   transitional

30

FIG. 13. *SH* synthetics for 2-D models with abrupt and transitional boundaries between the alluvium and rock (see text). Source-receiver configuration is the same as for the synthetics in Figure 12. Source depth is 5 km.

ics show that the duration of shaking is a strong function of position in the basin, with sites near the edge having less duration than sites in the middle of the basin. Probably the most important feature is the conversion of incident S waves to surface waves at the edges of the basin. This has been previously

reported for 2-D simulations, but the 3-D simulation illustrates how the wave-fronts are distorted and scattered by the irregular bedrock topography. The 3-D simulation also shows that body-to-surface-wave conversion occurs not only at the southern edge of the valley but also at the northeast edge. The results of the simulation qualitatively explain the presence of surface waves in the observed seismograms from the Sunnyvale dense array and the variability in back-azimuth observed for later arrivals in these seismograms (see Frankel et al., 1991). The prolonged duration of shaking due to these surface waves increases the seismic hazards to long-period structures located in sedimentary basins, such as highway overpasses, tall buildings, and pipelines. Therefore, synthetic seismograms from 3-D simulations should, in the future, have an important role to play in the design of such structures.

We have shown that large-scale 3-D simulations are computationally feasible for realistic basin models. A major limitation is the lack of detailed, 3-D velocity models for many basins of interest. There is a critical need for a more detailed model of the Santa Clara valley, if progress is to be made on matching the observed waveforms and predicting shaking for future earthquakes using 3-D simulations. The depth of the alluvium in the Santa Clara valley is not known except along the edges of the basin. This makes it impossible to predict the dominant periods of multiple body-wave reflections and surface waves. Analysis of the dense array data for the Loma Prieta aftershocks indicated surface-wave arrivals coming from the southeast starting about 10 sec after the direct S wave (Frankel et al., 1991). The east–west synthetic at SUN contain surface-wave arrivals from the east, but only at much later times of 24 sec after the S wave (Fig. 11a). It is possible that the early, observed surface wave arrivals were scattered from some feature located northwest of Oak Hill. There is aeromagnetic evidence that the material that comprises Oak Hill extends northwestward under the alluvium (see Brabb and Hanna, 1981). This material may form a horst under the central part of the basin (E. Helley, personal comm., 1990), which could scatter surface waves. Clearly, seismic refraction and reflection studie are needed to develop a model for the basin sufficiently accurate to predict ground motions for future earthquakes, based on 3-D simulations.

REFERENCES

Aki, K. and K. L. Larner (1970). Surface motion of a layered medium having an irregular interface due to incident plane SH waves, J. Geophys. Res. 75, 933–954.
Aki, K. and P. G. Richards (1980). Quantitative Seismology. W. H. Freeman, San Francisco.
Alford, R. M., K. R. Kelley, and D. M. Boore (1974). Accuracy of finite-difference modeling of the acoustic wave equation, Geophysics 39, 834–842.
Alterman, Z. S. and F. C. Karal, Jr. (1968). Propagation of elastic waves in layered media by finite-difference methods, Bull. Seism. Soc. Am. 58, 367–398.
Alterman, Z. S. and A. Rotenberg (1969). Seismic waves in a quarter plane, Bull. Seism. Soc. Am. 59, 347–368.
Bard, P. Y. and M. Bouchon (1980a). The seismic response of sediment-filled valleys. Part 1. The case of incident SH waves, Bull. Seism. Soc. Am. 70, 1263–1286.

Bard, P. Y. and M. Bouchon (1980b). The seismic response of sediment-filled valleys. Part 2. The case of incident P and SV waves, *Bull. Seism. Soc. Am.* **70**, 1921–1941.

Bard, P. Y. and M. Bouchon (1985). The two-dimensional resonance of sediment-filled valleys, *Bull. Seism. Soc. Am.* **75**, 519–542.

Bard, P. Y., M. Campillo, F. J. Chaves-Garcia, and F. J. Sanchez-Sesma (1988). The Mexico earthquake of September 19, 1985: a theoretical investigation of large and small-amplification effects in the Mexico City valley, *Earthquake Spectra* **4**, 609–633.

Boore, D. M. and J. Boatwright (1984). Average body-wave radiation coefficients, *Bull. Seism. Soc. Am.* **74**, 1615–1621.

Borcherdt, R. D. and J. F. Gibbs (1976). Effects of local geological conditions in the San Francisco Bay region on ground motions and the intensities of the 1906 earthquake, *Bull. Seism. Soc. Am.* **66**, 467–500.

Brabb, E. E. and W. F. Hanna (1981). Maps showing aeromagnetic anomalies, faults, earthquake epicenters, and igneous rocks in the southern San Francisco Bay region, California. U.S. Geol. Surv. Geophys. Invest. Map GP-California Department of Water Resources (1967). Evaluation of ground water resources, South San Francisco Bay, Appendix A, Geology, Bulletin 118-1.

California Division of Mines and Geology (1969). *Geologic Atlas of California*, CDMG, Sacramento.

Clayton, R. and B. Engquist (1977). Absorbing boundary conditions for acoustic and elastic wave equations, *Bull. Seism. Soc. Am.* **67**, 1529–1540.

Dietz, L. D. and W. L. Ellsworth (1990). The October 17, 1989, Loma Prieta, California, earthquake and its aftershocks: geometry of the sequence from high-resolution locations, *Geophys. Res. Lett.* **17**, 1417–1420.

Frankel, A., S. Hough, P. Friberg, and R. Busby (1991). Observations of Loma Prieta aftershocks from a dense array in Sunnyvale, California, *Bull. Seism. Soc. Am.* **81**, 1900–1922.

Harmsen, S. and S. Harding (1981). Surface motions over a sedimentary boundary for incident plane P and SV waves, *Bull. Seism. Soc. Am.* **71**, 655–670.

Haskell, N. A. (1960). Crustal reflection of plane SH waves, *J. Geophys. Res.* **65**, 4147–4150.

Hazlewood, R. M. (1976). Contour map and interpretive cross sections showing depth and configuration of bedrock surface, south San Francisco Bay region, California, U.S. Geol. Surv. Misc. Field Studies Map MF-796.

Joyner, W. B., R. E. Warrick, and T. E. Fumal (1981). The effect of Quaternary alluvium on strong ground motion in the Coyote Lake, California earthquake of 1979, *Bull. Seism. Soc. Am.* **71**, 1333–1349.

Joyner, W. B., R. E. Warrick, and A. A. Oliver III (1976). Analysis of seismograms from a downhole array in sediments near San Francisco Bay, *Bull. Seism. Soc. Am.* **66**, 937–958.

Kanai, K. (1952). Relation between the nature of surface layer and the amplitudes of earthquake motions, *Bull. Earthquake Res. Inst., Tokyo Univ.* **30**, 31–37.

Kawase, H. and K. Aki (1989). A study on the response of a soft basin for incident S, P, and Rayleigh waves with special reference to the long duration observed in Mexico City, *Bull. Seism. Soc. Am.* **79**, 1361–1382.

Kelly, F. C., R. W. Ward, S. Treitel, and R. M. Alford (1976). Synthetic seismograms: a finite-difference approach, *Geophysics* **41**, 2–27.

Mooney, W. D. and R. H. Colburn (1985). A seismic-refraction profile across the San Andreas, Sargent, and Calaveras Faults, west-central California, *Bull. Seism. Soc. Am.* **75**, 175–191.

Mueller, C. and G. Glassmoyer (1990). *Digital recordings of aftershocks of the 17 October 1989 Loma Prieta, California, earthquake, U.S. Geol. Surv. Open-File Rept. 90-503.*

Ohtsuki, A. and K. Harumi (1983). Effect of topographies and subsurface inhomogeneities on seismic SV waves, *Earthquake Eng. Struct. Dyn.* **11**, 444–461.

Oppenheimer, D. H. (1990). Aftershock slip behavior of the 1989 Loma Prieta, California earthquake, *Geophys. Res. Lett.* **17**, 1203–1206.

Rial, J. A. (1989). Seismic wave resonances in 3D sedimentary basins, *Geophys. J. Int.* **99**, 81–90.

Saikia, C. and M. Sen (1989). Long range and high-frequency synthetic seismograms using 1-D techniques, *EOS* **70**, 1200–1201.

Saito, M. (1967). Evaluation of free oscillations and surface waves by a point source in a vertically heterogeneous Earth, *J. Geophys. Res.* **72**, 3689–3699.

Sánchez-Sesma, F. J. (1983). Diffraction of elastic waves by three-dimensional surface irregularities, *Bull. Seism. Soc. Am.* **73**, 1621–1636.

Sánchez-Sesma, F. J., L. E. Pérez-Rocha, and S. Chávez-Perez (1989). Diffraction of elastic waves by three-dimensional surface irregularities. Part II. *Bull. Seism. Soc. Am.* **79**, 101–112.

A. FRANKEL AND J. VIDALE

Vidale, J. E. (1990). Comment on "A comparison of finite-difference and Fourier method calculations of synthetic seismograms" by C. R. Daudt *et al.*, *Bull. Seism. Soc. Am.* **80**, 493–495.

Vidale, J. E. and R. W. Clayton (1986). A stable free-surface boundary condition for 2-D elastic finite-difference wave simulation, *Geophysics* **51**, 2247–2249.

Vidale, J. E. and D. V. Helmberger (1988). Elastic finite-difference modeling of the 1971 San Fernando, California earthquake, *Bull. Seism. Soc. Am.* **78**, 122–141.

U.S. GEOLOGICAL SURVEY
922 NATIONAL CENTER
RESTON, VIRGINIA 22092
  (A.F.)

U.S. GEOLOGICAL SURVEY
345 MIDDLEFIELD ROAD
MENLO PARK, CALIFORNIA 94025
  (J.V.)